Solid-State Structures

Deutsche Ausgabe: DOI: 10.1002/ange.201502320
Internationale Ausgabe: DOI: 10.1002/anie.201502320

Frenkel-Defect-Mediated Chemical Ordering Transition in a Li–Mn–Ni Spinel Oxide**

*Hyewon Ryoo, Hyung Bin Bae, Young-Min Kim, Jin-Gyu Kim, Seongsu Lee, and Sung-Yoon Chung**

Abstract: *Using spinel-type $Li(Mn_{1.5}Ni_{0.5})O_4$ with two different cations, Mn and Ni, in the oxygen octahedra as a model system, we show that a cation ordering transition takes place through the formation of Frenkel-type point defects. A series of experimental results based on atomic-scale observations and in situ powder diffractions along with ab initio calculations consistently support such defect-mediated transition behavior. In addition to providing a precise suggestion of the intermediate transient states and the resulting kinetic pathway during the transition between two phases, our findings emphasize the significant role of point defects in ordering transformation of complex oxides.*

Identification and subsequent control of the chemical ordering in multi-component crystalline systems have been among the central issues in structural chemistry during several decades. As reviewed by Nix and Shockley[1] in 1938, a number of binary metallic alloys serve as prototypical examples that straightforwardly demonstrate how the degree of chemical order affects the resultant physical properties, such as electrical resistivity, magnetic susceptibility, and plastic deformation behavior of crystals. In addition to the ordering structures determined in bulk, many notable studies have been extended even to the elucidation of local chemical ordering (or clustering)[2–4] and visualization of atomic-scale antisite exchange disordering.[5–9]

[*] H. Ryoo, Prof. S.-Y. Chung
Graduate School of EEWS
Korea Advanced Institute of Science and Technology (KAIST)
Daejeon 305-338 (Korea)
E-mail: nalphates@gmail.com
sychung@kaist.ac.kr
Homepage: https://sites.google.com/site/atomicscaledefects/
H. B. Bae
KAIST Analysis Center
Korea Advanced Institute of Science and Technology (KAIST)
Daejeon 305-338 (Korea)
Dr. Y.-M. Kim, Dr. J.-G. Kim
Korea Basic Science Institute, Daejeon 305-806 (Korea)
Dr. S. Lee
Korea Atomic Energy Research Institute, Daejeon 305-353 (Korea)

[**] This work was supported by the National Research Foundation of Korea (NRF), grant numbers 2014R1A4A1003712 (BRL Program), 2013R1A1A2005243, and 2010-0028973. Y.M.K. and S.L. were also financially supported by the internal research program at the KBSI (grant number T34429) and the Nuclear R&D Program through the NRF (grant number 2012M2A2A6002461), respectively.

Supporting information for this article is available on the WWW under http://dx.doi.org/10.1002/anie.201502320.

In contrast to metallic alloys, many ionic oxides have a structural feature based on metal cations occupied at the oxygen interstitial sites in a close-packed oxygen anion framework. $A_xB_yO_z$-type complex oxides with multiple cations can thus show a variety of chemical ordering between cations at the *A* or *B* sites.[10–18] In particular, the precise determination of ordering structures between cations at each interstitial site as well as intersite mixing is imperative in AB_2O_4-type spinels, where cations occupy both one-eighth of the tetrahedral *A* sites and one-half of the octahedral *B* sites in a face-centered-cubic (FCC) oxygen sublattice, as these ordering structures are critical factors governing high-temperature chemical stability, magnetic properties, and electrochemical performance.[16–21]

Despite such a wide spectrum of research on the ordering structures in various complex oxides, precise information regarding the kinetic pathway for chemical ordering and the transient states during the ordering transformation remains elusive. As an appropriate model system to observe an ordering transition, we chose $Li(Mn_{1.5}Ni_{0.5})O_4$ spinel, where a typical *B*-site configurational ordering between Mn and Ni takes place at 700 °C.[22,23] Our study critically reveals that the ordering transition occurs through the formation of Frenkel-type defects, which entail the displacement of Mn and Ni from their normal *B* sites onto vacant octahedral interstitials in the lattice. Experimental and computational details are provided in the Supporting Information.

Disordered $Li(Mn_{1.5}Ni_{0.5})O_4$, which is usually synthesized at 900 °C, transforms into an ordered phase when it is post-annealed at 700 °C. The ordered phase reveals a periodic Ni arrangement among the *B* sites as a at low temperature stable configuration (space group $P4_332$; see Movie S1 in the Supporting Information for structural features), while the disordered phase having a random distribution of Ni (space group $Fd\bar{3}m$) is thermodynamically stable at high temperature above 800 °C.[22,23] To scrutinize structural variations at atomic resolution during the initial stage of chemical ordering, we prepared a polycrystalline specimen by re-annealing at 700 °C for a short time (2 h) after the primary synthesis at 900 °C. Figure 1a shows a [101]-projection high-resolution electron microscopy (HREM) image of a $Li(Mn_{1.5}Ni_{0.5})O_4$ crystal from the post-annealed specimen along with two fast Fourier transforms (FFTs) of the nanoscale regions indicated by light-blue and pink rectangles, respectively. Because the atomic numbers *Z* of Mn ($Z=25$) and Ni ($Z=28$) are not substantially different, it is very difficult to discriminate the variation of the lattice fringe in phase-contrast HREM images (left insets) between the ordered and the disordered phases (see Figure S1 in the Supporting Information). However, the

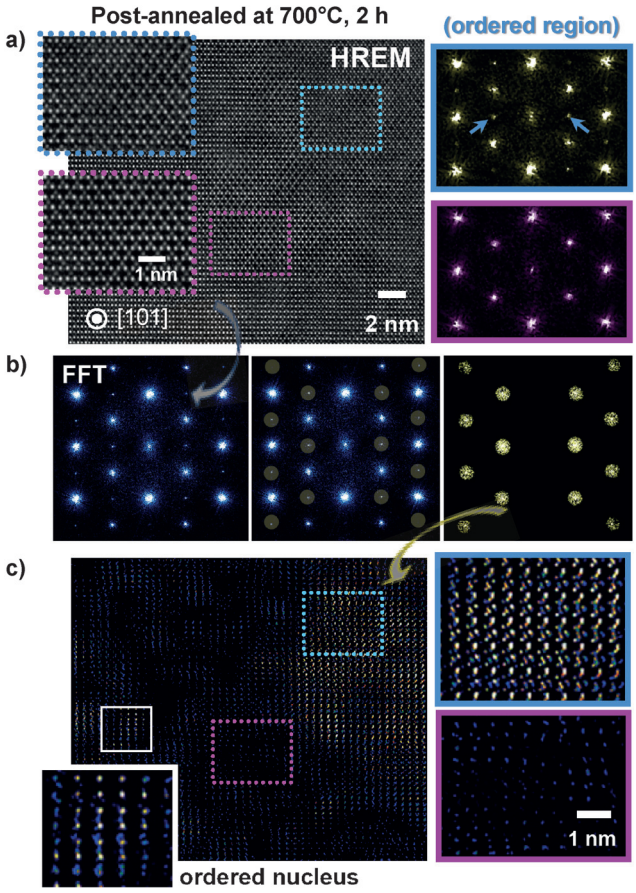

Figure 1. Phase-contrast HREM images and inverse FFTs of $Li(Mn_{1.5}Ni_{0.5})O_4$ post-annealed at 700 °C for 2 h. a) Two enlargements of the regions denoted by light-blue and pink rectangles in the HREM image show no substantial difference in lattice fringe. In contrast, additional Bragg spots are identified in the FFT of the light-blue region, demonstrating the occurrence of ordering. b) Yellow masks (middle) are applied in the FFT obtained from the entire HREM image (left) to selectively filter the superlattice peaks only (right). c) A Fourier-filtered image is constructed from the masked yellow FFT shown in (b). Lattice fringes stemming from the ordering structure are revealed, as shown in the enlargement (light blue), while no significant fringes are observed in the disordered regions (pink).

periodic arrangement of Ni in the *B* sites leads to the appearance of additional Bragg spots in electron diffraction patterns and FFTs of HREM images (see Figure S2). While no additional Bragg spots appear in the FFT for the pink region, superlattice spots are clearly identified in the FFT of the blue regions, as indicated by arrows, directly verifying that *B*-site ordering has occurred in this region. A video clip of live FFTs captured in CRISP[24] is included in Movie S2 to clarify the appearance and extinction of the superlattice spots and thus exhibit the co-existence of the two phases in a crystal.

In order to construct a lattice image selectively distinguishing the ordered regions, we carried out an inverse Fourier transform of the superlattice spots in the FFT. The left blue FFT in Figure 1b was obtained from the entire HREM image shown in Figure 1a. The additional Bragg spots in the FFT could be filtered by applying circular masks on them (middle), resulting in the ordering superlattice FFT in yellow (right). Figure 1c shows a Fourier-filtered lattice image, revealing the local evolution of the ordering transition. From a comparison of the magnified images on the right-hand side, the light-blue region, which shows the superlattice Bragg spots in the FFT of Figure 1a, consistently demonstrates a well-developed image feature verifying the occurrence of an ordering transition, whereas a significant fringe cannot be observed in the disordered pink region. A notable aspect from the overview image of Figure 1c is that nanodomains showing a substantial ordering fringe are frequently observed as small nuclei, as indicated by a white rectangle. An extra set of FFTs and a resulting Fourier filtered image are also provided in Figure S3 to confirm this transition behavior.

One of the key findings of our study was obtained from the atomic column-by-column analysis using high-angle annular dark-field (HAADF) scanning transmission electron microscopy (STEM). Figure 2a shows a HAADF-STEM image along with an enlargement of the image in the [101] projection of a disordered $Li(Mn_{1.5}Ni_{0.5})O_4$ crystal with $Fd\bar{3}m$ symmetry. Mn and Ni are randomly distributed onto the octahedral interstitials, *16d* sites in the Wyckoff position (see Table S1), leaving the other octahedral interstitials, *16c* sites, empty. Consequently, the atomic columns consisting

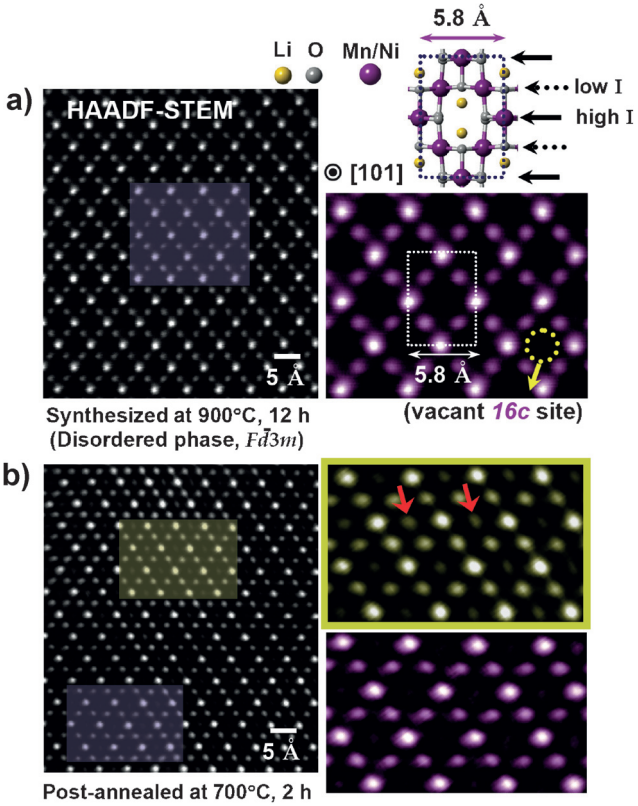

Figure 2. HAADF-STEM images in the [101] projection. a) The columns consisting of the *16c* sites only, as denoted by a yellow circle, have no image intensity, whereas the *16d*-site columns show the brightest image feature in disordered $Li(Mn_{1.5}Ni_{0.5})O_4$. The columns with relatively low intensity are mixed with the Mn/Ni containing *16d* and empty *16c* sites. b) In a specimen post-annealed at 700 °C, some of the vacant *16c*-site columns exhibit detectable image intensity, indicating the displacement of Mn/Ni from the *16d* sites, as shown in the enlargement in yellow.

of *16d* sites exhibit the highest intensity in the HAADF-STEM image, whereas the columns of empty *16c* sites show no brightness. In clear contrast, significant intensity was frequently detected in the vacant *16c*-site columns during the STEM analysis of the boundary areas between highly ordered and disordered regions in the crystals post-annealed at 700 °C for 2 h. When the enlargement of the yellow-shadow region is compared with that of the purple-shadow region in Figure 2b, sufficiently detectable intensities in some of the *16c*-site columns, for example those indicated by red arrows, can be verified in the HAADF-STEM image. This observation directly shows that the displacement of Mn and Ni from *16d* sites into vacant *16c* sites has occurred during the ordering transition, representing the formation of Frenkel-type defects.

An electron beam accelerated with a high voltage in a transmission electron microscope can transfer sufficient energy to a specimen, and on this basis this approach has been properly used in recent in situ studies for real-time observations regarding phase transformation[25,26] and diffusion of atoms[27] without additional heating. To induce the atomic displacement process and subsequently examine the formation of Frenkel-type defects, we applied an intensified convergent electron beam on narrow regions in a disordered crystal in STEM. While no structure variation was observed during scanning with electrons in normal imaging mode (see Movie S3), we could identify dynamic fluctuation in the column intensity between the octahedral *16d* and *16c* sites when an electron beam with a higher current (>50 pA) scanned a confined region of 3×3 nm^2. A series of in situ HAADF-STEM images in Figure 3 clearly show that a substantial intensity in an initially empty *16c* column (red arrow) appears at 21 seconds and reappears at 29 seconds after the extinction at 25 seconds. Analogous oscillatory behavior of the intensity variation is also verified in another *16c* column (blue arrow) in the present series. Movie S4 demonstrates this dynamic aspect of the column intensity in real time. More specific intensity fluctuations originating from the motion of Mn and Ni between atomic columns can be confirmed in Movie S5. Based on a previous report on electron-beam-induced atom diffusion,[27] we have provided a quantitative estimation regarding the energy transfer from accelerated electrons to Mn and Ni atoms under the assumption of purely elastic collisions in Figure S4.

In situ X-ray powder diffraction was carried out at high temperature to macroscopically examine the formation of Frenkel-type defects during the ordering transition. Prior to performing the powder diffraction experiment, plausible diffraction patterns were calculated when some of the vacant *16c* sites were filled with Mn/Ni atoms in ($2a\times2a\times2a$) supercells of $Fd\bar{3}m$ symmetry (see Figure S5 for construction of the supercells). As denoted by asterisks in Figure 4a, additional diffraction peaks around the major (111) reflection can be identified and their intensities proportionally increase to a fraction of occupancy at the *16c* sites, showing that the peak indicated by a black arrow at 18.05° has the highest intensity as a main shoulder.

Figure 4b shows a series of X-ray diffraction patterns experimentally collected in real time when a completely

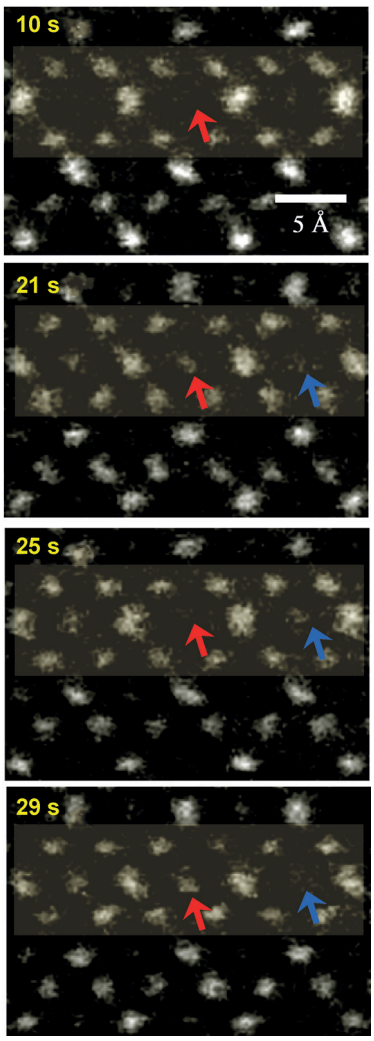

Figure 3. Series of HAADF-STEM images showing Mn/Ni migrations. This series was captured from the video clip in Movie S4. As indicated by red arrows, substantial column intensity is repeatedly detected at the empty *16c* sites, for example, at 21 and 29 s. Another column indicted by blue arrows shows the same behavior in intensity variation induced by an electron beam.

disordered $Li(Mn_{1.5}Ni_{0.5})O_4$ powder sample was annealed at 700 °C for 4 h to induce Mn/Ni ordering in a hot-stage diffractometer. The most notable feature in this series is the emergence of a shoulder peak with substantial intensity around the (111) reflection, in agreement with the calculated patterns, as indicated by a black arrow with a gray background. The other small peaks were not distinguishable from the background noise during collection of the X-ray signals at high temperature. Furthermore, the intensity of this shoulder is found to fluctuate somewhat with the annealing time. As shown by a gray background in Figure 4b, this shoulder is scarcely detectable, for example, at 130–150 minutes, in contrast to the clear discrimination at 210–220 minutes, demonstrating the dynamic formation and extinction of Frenkel-type defects during ordering.

Formation of point defects in a crystal is a thermally activated process. Consequently, such a defective high-energy

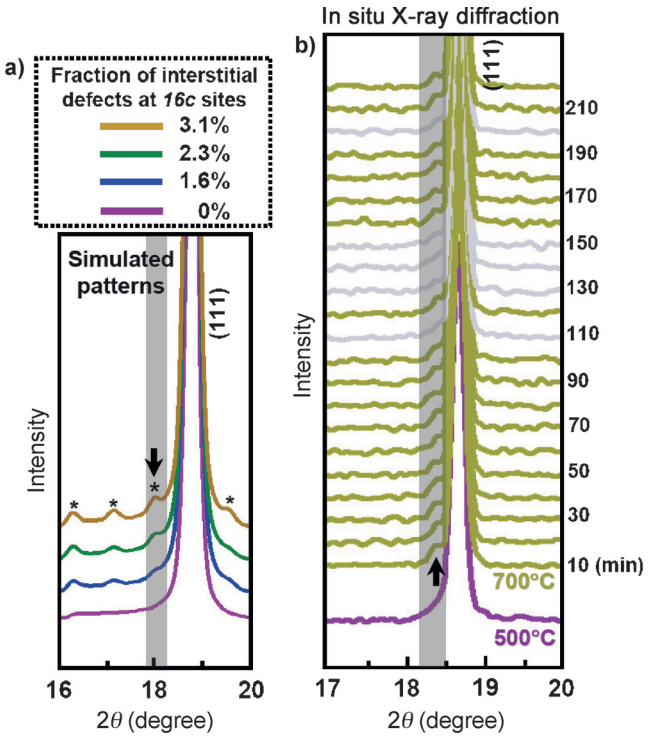

Figure 4. Simulated and experimentally collected X-ray diffraction patterns. a) Simulated diffraction patterns near the (111) Bragg reflection are presented. The intensity of the extra peaks denoted by asterisks becomes higher as the fraction of occupancy by Mn/Ni at the vacant *16c* sites increases. The black arrow with the gray background indicates the highest-intensity peak. b) While a powder sample with disordered structure shows no extra shoulder at 500 °C, the appearance of the additional shoulder peak is identified during collection of diffraction signals at 700 °C, as indicated by the black arrow.

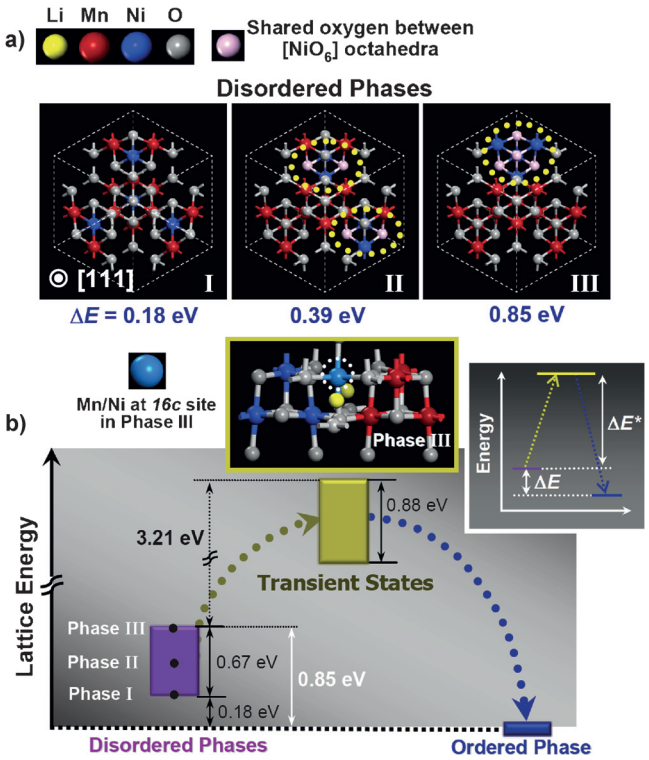

Figure 5. DFT calculations and energy landscape for ordering transition. a) Three disordered structures with different Ni configurations are exemplified as phases I, II, and III. b) The overall energy landscape is given to suggest relative energy differences between the disordered phases (purple), the transient states (yellow), and the ordered phase (blue). A structure of phase III with a Frenkel defect (sky-blue sphere) is illustrated as an example of a transient state. The inset schematically depicts the much larger activation barrier (ΔE^*) compared with the driving force (ΔE) of the ordering transition.

state is not attainable unless sufficient energy is supplied to overcome the activation barrier. As shown in the purple pattern of Figure 4b, the shoulder peak stemming from the *16c*-site occupancy thus does not appear during annealing at a lower temperature of 500 °C. The in situ STEM results shown in Movies S3 and S4 also consistently support the presence of an energy barrier during the transition. In addition to these experimental results, we carried out DFT calculations in the CASTEP code (the GGA-PBEsol functional and a plane-wave cutoff energy of 500 eV) to quantitatively suggest an energy landscape between the ordered/disordered phases and the transient states associated with the Frenkel defect formation.

The relative energy difference, ΔE, of the disordered phases with respect to that of the ordered phase is defined as $\Delta E = E(\text{disordered phase}) - E(\text{ordered phase with } P4_332 \text{ symmetry})$, where E is the lattice enthalpy of a unit cell after geometry optimization in each case. We constructed six unit cells having a different type of Ni disordering that deviates from the $P4_332$ symmetry for the calculations (see Figures S6 and S7). Each lattice enthalpy of the six cells shows a systematic increment as the four $[NiO_6]$ octahedra come closer to each other (see Table S2 for the geometric relationship along with the ΔE values). Three cells out of the six are exemplified as disordered phases I, II, and III in Figure 5a. While phase I, which has isolated $[NiO_6]$ octahedra, presents the lowest ΔE, phase III with complete clustering of the four $[NiO_6]$ units shows the highest ΔE value, indicating that the energy difference per unit cell between the ordered and disordered phases ranges from 0.18 to 0.85 eV. The formation energies of Frenkel-type defects, which are formed by the displacements of Mn and Ni onto the empty *16c* sites, were also calculated in disordered phases I, II, and III to estimate the relative energy status of the transient states. Although there is some variation among the values, the defect formation energies are in a range of 2.58–3.67 eV (see Table S3 for a detailed list). Consequently, the overall energy landscape during the ordering transition is depicted as shown in Figure 5b.

This combination of DFT calculations and various experimental analyses allows us to understand several features concerning the ordering transition in $Li(Mn_{1.5}Ni_{0.5})O_4$ spinel. First, as schematically described in the right inset of Figure 5b, the energy barrier, ΔE^*, during this transition is larger than the driving force, ΔE, for the transformation. Fairly sluggish transition kinetics therefore appears unavoidable. In fact, when we observed $Li(Mn_{1.5}Ni_{0.5})O_4$ crystals after post-annealing at 700 °C even for 120 h, disordered nanoscale regions that remain untransformed were still found on

HREM and inverse FFT analyses (see Figures S8 and S9 for lattice-fringe images). Second, our additional DFT calculations show that the activation energies for vacancy migration of Mn and Ni between the regular Mn/Ni positions (*16d* sites) are less than 2 eV (see Figure S10). This indicates that the rate-limiting step during the ordering transition is the formation of Frenkel-type defects; once the displacement of a sufficient number of Mn/Ni atoms onto the empty *16c* sites occurs, the rearrangement for cation ordering by vacancy migration between regular *16d* octahedral sites is achieved with much lower activation energies. Furthermore, a sufficient amount of atomic vacancies at the *16d* sites is believed to be necessary for Mn/Ni to easily rearrange by migration and thereby trigger the nucleation of $P4_332$-symmetry ordering from a geometrical viewpoint.

In summary, we have demonstrated that the *B*-site configurational ordering in a AB_2O_4-type spinel oxide, $Li(Mn_{1.5}Ni_{0.5})O_4$, takes place through the formation of Frenkel defects at octahedral sites as a crucial transient state. As such defect formation entails both cation interstitials at the empty oxygen octahedra and vacancies at the regular *B* sites, the rearrangement of the *B*-site cations towards a stable ordering configuration can be effectively achieved by transient displacement of cations onto the empty octahedra and subsequent vacancy migration at the *B* sites. The present study emphasizes that the role of point defects in crystals is not confined merely to mass and charge transport in general but extends even to phase transitions, where these defects act as a critical mediator between two phases.

Keywords: defects · electron microscopy · phase transitions · solid-state structures · spinel phases

How to cite: *Angew. Chem. Int. Ed.* **2015**, *54*, 7963 – 7967
Angew. Chem. **2015**, *127*, 8074 – 8078

[1] F. C. Nix, W. Shockley, *Rev. Mod. Phys.* **1938**, *10*, 1 – 71.
[2] M. Gu, I. Belharouak, A. Genc, Z. Wang, D. Wang, K. Amine, F. Gao, G. Zhou, S. Thevuthasan, D. R. Baer, J.-G. Zhang, N. D. Browning, C. Wang, *Nano Lett.* **2012**, *12*, 5186 – 5191.
[3] D. Wang, H. L. Xin, R. Hovden, H. Wang, Y. Yu, D. A. Muller, F. J. DiSalvo, H. D. Abruña, *Nat. Mater.* **2013**, *12*, 81 – 87.
[4] C. Cui, L. Gan, M. Heggen, S. Rudi, P. Strasser, *Nat. Mater.* **2013**, *12*, 765 – 771.
[5] a) S.-Y. Chung, S.-Y. Choi, T. Yamamoto, Y. Ikuhara, *Phys. Rev. Lett.* **2008**, *100*, 125502; b) S.-Y. Chung, S.-Y. Choi, T. Yamamoto, Y. Ikuhara, *Angew. Chem. Int. Ed.* **2009**, *48*, 543 – 546; *Angew. Chem.* **2009**, *121*, 551 – 554.
[6] a) S.-Y. Chung, S.-Y. Choi, S. Lee, Y. Ikuhara, *Phys. Rev. Lett.* **2012**, *108*, 195501; b) S.-Y. Chung, S.-Y. Choi, T.-H. Kim, S. Lee, *ACS Nano* **2015**, *9*, 850 – 859.
[7] Y. Jiang, Y. Wang, J. Sagendorf, D. West, X. Kou, X. Wei, L. He, K. L. Wang, S. Zhang, Z. Zhang, *Nano Lett.* **2013**, *13*, 2851 – 2856.
[8] F. Lin, I. M. Markus, D. Nordlund, T.-C. Weng, M. D. Asta, H. L. Xin, M. M. Doeff, *Nat. Commun.* **2014**, *5*, 3529.
[9] H. Dixit, W. Zhou, J.-C. Idrobo, J. Nanda, V. R. Cooper, *ACS Nano* **2014**, *8*, 12710 – 12716.
[10] E. Pollert, *React. Solids* **1988**, *5*, 279 – 291.
[11] S.-Y. Choi, S.-Y. Chung, T. Yamamoto, Y. Ikuhara, *Adv. Mater.* **2009**, *21*, 885 – 889.
[12] W. Dachraoui, T. Yang, C. Liu, G. King, J. Handermann, G. Van Tendeloo, A. Liobet, M. Greenblatt, *Chem. Mater.* **2011**, *23*, 2398 – 2406.
[13] S. García-Martín, E. Urones-Garrote, M. C. Knapp, G. King, P. M. Woodward, *J. Am. Chem. Soc.* **2008**, *130*, 15028 – 15037.
[14] B. S. Guiton, P. K. Davies, *J. Am. Chem. Soc.* **2008**, *130*, 17168 – 17173.
[15] S. García-Martín, G. King, E. Urones-Garrote, G. Nénert, P. M. Woodward, *Chem. Mater.* **2011**, *23*, 163 – 170.
[16] T. Maiyalagan, K. A. Jarvis, S. Therese, P. J. Ferreira, A. Manthiram, *Nat. Commun.* **2014**, *5*, 3949.
[17] D. Tang, Y. Sun, Z. Yang, L. Ben, L. Gu, X. Huang, *Chem. Mater.* **2014**, *26*, 3535 – 3543.
[18] M. A. Willard, Y. Nakamura, D. E. Laughlin, M. E. McHenry, *J. Am. Ceram. Soc.* **1999**, *82*, 3342 – 3346.
[19] J.-H. Kim, S.-T. Myung, C. S. Yoon, S. G. Kang, Y.-K. Sun, *Chem. Mater.* **2004**, *16*, 906 – 914.
[20] E.-S. Lee, K.-W. Nam, E. Hu, A. Manthiram, *Chem. Mater.* **2012**, *24*, 3610 – 3620.
[21] J.-H. Kim, A. Huq, M. Chi, N. P. W. Pieczonka, E. Lee, C. A. Bridges, M. M. Tessema, A. Manthiram, K. A. Persson, B. R. Powell, *Chem. Mater.* **2014**, *26*, 4377 – 4386.
[22] D. Pasero, N. Reeves, V. Pralong, A. R. West, *J. Electrochem. Soc.* **2008**, *155*, A282 – A291.
[23] L. Cai, Z. Liu, K. An, C. Liang, *J. Mater. Chem. A* **2013**, *1*, 6908 – 6914.
[24] X. Zou, S. Hovmöller, *Acta Crystallogr. Sect. A* **2008**, *64*, 149 – 160.
[25] H. Zheng, J. B. Rivest, T. A. Miller, B. Sadtler, A. Lindenberg, M. F. Toney, L.-W. Wang, C. Kisielowski, A. P. Alivisatos, *Science* **2011**, *333*, 206 – 209.
[26] L. Yao, S. Majumdar, L. Äkäslompolo, S. Inkinen, Q. H. Qin, S. van Dijken, *Adv. Mater.* **2014**, *26*, 2789 – 2793.
[27] R. Ishikawa, R. Mishra, A. R. Lupini, S. D. Findley, T. Taniguchi, S. T. Pantelides, S. J. Pennycook, *Phys. Rev. Lett.* **2014**, *113*, 155501.

Received: March 12, 2015
Published online: May 26, 2015

